ELSEVIER

Materials Science and Engineering A279 (2000) 149–159

MATERIALS SCIENCE & ENGINEERING A

www.elsevier.com/locate/msea

On the local microstructural characteristics observed in sand cast Al–Si alloys

C. González-Rivera [a,*], B. Campillo [a], M. Castro [b], M. Herrera [b], J. Juárez-Islas [c]

[a] *Departamento de Ingeniería Metalúrgica, Facultad de Química, UNAM, Circuito Exterior S/N, Edif. 'D', Cd. Universitaria, 04510, Mexico D.F., Mexico*

[b] *CINVESTAV-IPN Unidad Saltillo, Carr. Saltillo-Monterrey Km 13, 25000, Saltillo Coahuila, Mexico*

[c] *Instituto de Investigaciones en Materiales, UNAM, Circuito Exterior S/N, Cd. Universitaria, 04510, Mexico D.F., Mexico*

Received 15 March 1999; received in revised form 8 September 1999

Abstract

The aim of this work is to explore the phenomenology that describes the local solid formation and heat transfer occurring during sand cast alloys solidification in order to propose an explanation to the observed changes of local microstructural characteristic lengths in hypoeutectic and eutectic Al–Si based alloys. Microstructural observations are made in different radial positions of solidified rod castings. Also, solidification kinetics information is obtained using the Fourier thermal analysis method. A coupled heat transfer-solidification kinetics model is employed to predict the thermal history, the solidification kinetics and some microstructural parameters in order to compare the predictions with experimental results. The model and the experimental outcome suggest that there is a strong dependence of the local solidification kinetics on the local heat transfer. The analysis of this dependence is used to propose an explanation to the observed changes in microstructural characteristics at different locations within sand castings.

Keywords: Solidification kinetics; Fourier thermal analysis; Microstructure; Al–Si alloys

1. Introduction

Modeling microstructure formation during solidification has become an important tool, so recent progress has been made in modeling, computing and processes simulation in order to enhance our physical understanding of solidification. Most of the efforts in this regard have included two main aspects: the modeling of kinetics of microstructure formation coupled to macroscopic transport phenomena [1]. The potentially significant savings in the time required for prototyping and in the cost associated with defective castings have been the major reason behind this attention [2]. Nowadays, progress has been made in modeling various aspects of alloy solidification as reported in [1–5]. Also some studies [6–10] have been directed towards the analysis of local solidification kinetics as influenced by the heat transfer process involved in casting and others have shown the consequences [7,10] of this influence on the microstructural characteristics observed in different locations within a casting. During equiaxed solidification [11], commonly found in several sand casting alloys, it is known [12] that the bath undercooling and the alloy composition are the processing variables that defines the microstructural characteristics observed in the solid product. For a specific alloy, the local undercooling present during solid formation controls the local solidification kinetics and the local microstructural lengths such as dendrite tip radius, secondary dendrite arm spacing or eutectic spacing, and the microstructural changes observed in different locations within a casting show the differences between the local solidification kinetics acting during the phase transformation. From this, it is of prime interest to explore the factors affecting the local solidification kinetics during any solidification process. The challenge is to understand the mechanisms and the roll of all the involved phenomena.

* Corresponding author. Tel.: +52-5-6225225; fax: +52-5-6224645.

E-mail address: carlosgr@servidor.unam.mx (C. González-Rivera)

0921-5093/00/$ - see front matter
PII: S0921-5093(99)00625-5

The verifications between model predictions and experimental results on local solidification kinetics can be properly addressed [6,10,13], by using the method of thermal analysis called the Fourier Thermal Analysis (FTA, [8]). This method allows the generation of solidification kinetics data from the numerical processing of the temperature measurements in two locations within a symmetric casting. The fundamental concepts and implementation of this method has been described elsewhere [8].

In this work, a modest beginning of an attempt has been made to understand the causes behind the changes of microstructural characteristics observed at different positions within Al–Si sand rod castings. Accordingly, the purpose of this work is: (i) to obtain experimental information on local solidification kinetics and microstructure of eutectic and hypoeutectic Al–Si cast alloys; (ii) to use a heat transfer-solidification kinetics model in order to compare the model predictions with experimental results which include cooling curves, microstructural characteristic lengths and local solidification kinetics; and (iii) to analyze the information obtained in order to propose an explanation to the observed changes of local microstructural characteristics within the castings.

2. Experimental

Pre-weighted quantities of an hypoeutectic and a near eutectic Al–Si alloy, designated as A_1 and A_2 alloy respectively, were melted into a resistance furnace under an argon atmosphere. The chemical composition of the alloys used in this work is given in Table 1. The alloys were degassed with argon during 8 min prior to pouring, and directly cast into a green sand mold with a cylindrical casting cavity of 0.016 m of internal diameter and 0.15 m in height (with an insulated top and bottom). In order to record the thermal history of the alloy during cooling, two 0.0003 m diameter bore, type K thermocouples, with alumina sheath, 0.0016 m OD, were introduced at the mid height of the sand mold cavity at two different distances from the center of the casting. The tip of the thermocouples was in direct contact with the alloys under study and the thermocouple outputs were recorded on a personal computer with data recording and processing facilities. The cooling curves obtained were numerically processed using the FTA method [8] in order to obtain information about the solidification kinetics of the region of the casting near to the inner thermocouple.

Table 1
Chemical composition of the alloys (in wt.%)

Alloy	% Si	% Fe	% Cu	% Mg	%Al
A_1	7.59	0.48	0.1	0.25	Balance
A_2	11.4	0.5	0.6	0.10	Balance

After solidification, the specimens were cut in halves in order to verify the positions of the thermocouples and a cross section of each specimen was polished for microstructural observation. Three zones of interest were considered during metallographic examinations of the cross section of the cylindrical probe: (1) center of the probe, at $r = 0$ m; (2) edge of the probe, at $r = 0.008$ m and (3) intermediate region, at $r = 0.004$ m. In the case of the hypoeutectic alloy, attention was focused on the secondary dendrite arm spacing, (SDAS), measured by applying the procedure shown in Ref. [14]. For the near eutectic alloy, attention was focused on the average interfacial distances between eutectic lamellae, and the mean interlamellar eutectic spacing was measured by using the method described in Ref. [15].

2.1. Solidification model

2.1.1. Heat transfer

During the cooling and solidification of the cylindrical casting in a sand mold, it is assumed that the macroscopic heat flow is governed by conductive heat transfer and latent heat generation due to solidification (i.e. convective effects are not considered). Also it is assumed a constant thermal conductivity and zero heat flux in the θ and Z directions for the cylindrical system. Then the energy balance applied to the metal/mold system can be written as:

$$Cp_j^{\mathrm{v}} \frac{\partial T(r,t)}{\partial t} = k_j^{\mathrm{th}} \frac{1}{r} \frac{\partial}{\partial r}\left(r \frac{\partial T(r,t)}{\partial r} \right) + L_{\mathrm{f}}^{\mathrm{v}} \frac{\partial f_{\mathrm{s}}(r,t)}{\partial t}$$

$$Q_{\mathrm{a}} = Q_{\mathrm{c}} + Q_{\mathrm{s}} \qquad (1)$$

where Cp^{v} is the volumetric heat capacity, $T(r, t)$ is the temperature, r is the radial position, t is the time, k^{th} is the thermal conductivity, $L_{\mathrm{f}}^{\mathrm{v}}$ is the volumetric heat of fusion and the subscript j indicates the metal domain ($j = 1$) or the mold domain ($j = 2$). To solve the Eq. (1), $f_{\mathrm{s}}(r, t)$, the solid fraction as a function of time and position within the casting must be described. The solidification kinetics model coupled to the heat transfer calculations provides this kind of information. The Eq. (1) was solved by generating a discretized description of the cylindrical metal/mold system in the form of a finite difference mesh composed by a known number of cylindrical volume elements (VE). When $j = 1$ (i.e. metal domain) and during solidification, the thermal history of a VE can be obtained from the evolution of the local heat flow accumulation term, Q_{a}, (see Eq. (1)), which in turn can be simulated through the knowledge of the net heat exchange of the VE to its surroundings, Q_{c}, and of the latent heat released as a result of local solidification, Q_{s}, during the computing time step. The

Table 2
Selected data used during simulation

Metal	
Nucleation and growth constants	
Dendritic grains	
$A = 3.75 \times 10^9$	m^{-3}
$B = 2.3 \times 10^7$	$s^2\ m^{-3}\ °C^2$
Eutectic grains	
$A = 5.21 \times 10^8$	m^{-3}
$B = 3.56 \times 10^6$	$s^2\ m^{-3}\ °C^2$
$\mu_E = 5 \times 10^{-6}$	$m\ s^{-1}\ °C^2$
Thermal conductivity[a]	
$k_l^{th} = 77.36$	$W\ m^{-1}\ °C$
$k_s^{th} = 122.26$	$W\ m^{-1}\ °C$
Thermal diffusivity[a]	
$\alpha_l = 3.19 \times 10^{-5}$	$m^2\ s^{-1}$
$\alpha_s = 5.5 \times 10^{-5}$	$m^2\ s^{-1}$
$\varphi = 2450$	$Kg\ m^{-3}$
$L_f = 9.5 \times 10^8$	$J\ m^{-3}$
$\Gamma = 0.9 \times 10^{-7}$	mK
$D_l = 3 \times 10^{-9}$	$m^2\ s^{-1}$
Sand mold	
$\varphi = 1500$	$kg\ m^{-3}$
Thermal conductivity (mold)	
$k^{th} = -5.54E-10T^3 + 1.88E-6T^2 - 1.48E-2T + 1.35$	$W\ m^{-1}\ °C$
Heat capacity (mold)	
$T > 600°C\ \ Cp = -9.51E-3T^2 + 1.19T + 740.69$	$J\ kg^{-1}\ °C$
$T < 600°C\ \ Cp = 1045.03 + 0.13T$	$J\ kg^{-1}\ °C$
$h = 20$	$W\ m^{-2}\ °C$

[a] Subscripts: l, liquid; s, solid.

Table 3
Equivalent binary alloy system parameters used for A_1 alloy

$\bar{m}_l$ (°C/%)	$\bar{k}_0$	$\bar{C}_0$ (%)	(%)
−6.32	0.124	8.42	1.85

Table 4
Selected partition coefficients and liquidus slopes

Element i	Partition coefficient k_i	Liquidus slope m_i	Ref.
Si	0.117	−6.58	[18]
Mg	0.42	−5.98	[14]
Fe	0.022	−2.95	[14]
Cu	0.17	−3.43	[14]

assumptions, including the initial and the boundary conditions used to solve Eq. (1) were described in a previous work [10].

2.1.2. Solidification kinetics

The model assumes that, as a result of solidification there are two main solidification products: (i) equiaxed dendrites of solid solution rich in aluminum, i.e. the primary phase formed between the liquidus temperature and the eutectic temperature; and (ii) eutectic microconstituent.

Two types of eutectic morphology form in unmodified Al–Si alloys: (a) independently nucleated equiaxed grains; and (b) eutectic which nucleates mostly on the primary phase. The former prevails in eutectic Al–Si alloy. The hypoeutectic alloys shows the two types of morphology, prevailing the latter type as the silicon content is decreased from the eutectic composition. For simplicity it was assumed that the eutectic present in the alloys under study shows equiaxed morphology, and the difference existing between the solidification kinetics of the eutectic formed in A_1 and A_2 alloys was included by using, in each case, different impingement treatments, as will be shown later.

The assumed instantaneous nucleation of the equiaxed dendritic and eutectic grains use a simple empirical nucleation law that correlates the number of nuclei and the cooling rate at the beginning of solidification by employing a parabolic equation of the form:

$$\hat{N} = A + B\left(\frac{\partial T}{\partial t}\right)^2_{T_{ss}} \quad (2)$$

where $\hat{N}$ is the nucleation site density and the constants A and B were experimentally determined from the grain density (number m^{-3}) versus cooling rate data. Grain density was obtained by measuring the number of grains by the mean intersection method on several probes of A_1 and A_2 alloys cooled at different cooling rates [16]. The temperatures, T_{ss}, at which the corresponding cooling rate was evaluated and associated to the measured nuclei density were the liquidus temperature, for the dendritic grains and the eutectic temperature, for the A_2 alloy eutectic grains. The nuclei density versus cooling rate data were plotted and a curve fitting technique was applied to obtain the parameters of the nucleation equations. The numerical parameters for the dendritic and the eutectic nucleation are shown in Table 2.

In order to take into account the multicomponent nature of the alloys used in this work, the multicomponent system was treated as an equivalent binary alloy system where aluminum is the solvent and there is an equivalent solute. The equivalent solute represents the contributions of the several solutes present in the multicomponent solution. The equivalent binary alloy system [17] has an associated phase diagram described by four parameters: the equivalent liquidus slope $\bar{m}_l$, the equivalent partition coefficient $\bar{k}_0$, the equivalent initial solute content $\bar{C}_0$, and the equivalent maximum solubility of solute in the solid solution rich in aluminum $\bar{C}_s^{max}$. The values used in the model for the A_1 alloy are shown in Table 3. These parameters were calculated using the expressions proposed by Wang et al. [17] and the data shown in Table 4.

In order to describe the dendritic grain growth during the primary phase solidification, a simple geometry model that relates the dendritic tip position with the thermal and solutal field in the metal domain during dendrite growth in an undercooled melt was implemented. This was achieved by applying to the hypoeutectic alloy of interest in this work, the procedure outlined by Wang et al. [17], where the LGK model [19] is extended from binary to multicomponent alloy systems and is used to link the dendrite tip velocity to the total undercooling. This procedure, which assumes a dendrite tip of the form described by a paraboloid of revolution which grows at a constant growth rate, shows that for a given alloy composition, and undercooling, ΔT_d, the dendritic growth rate, V_d, can be calculated satisfying simultaneously the transport equations for heat and solute around the dendrite tip, described by Eq. (7) in Ref. [17], and the condition of marginal stability included in Eq. (6) of Ref. [17]. Performing several calculations at different ΔT_d values enables the plotting of V_d versus ΔT_d data, and applying a curve fitting technique to this data yields an expression for the growth rate of the dendrite tip as a function of undercooling, associated to the multicomponent alloy. Accordingly, Eqs. (6) and (7) of Ref. [17] were simultaneously solved for different ΔT_d values by numerical methods, using the data shown in Tables 1, 2 and 4. In this way it was obtained an expression for the growth rate of the dendrite tip in the A_1 alloy as a function of dendritic undercooling, Eq. (3), which is used in the micro–macro modeling program to compute the dendrite growth rate in a multicomponent manner:

$$V_d = \frac{\partial R_d}{\partial t} = 7.52 \times 10^{-7} \Delta T_d^{2.85} \quad (3)$$

It is interesting to mention that expressions of the type $V_d = B\Delta T_d^b$ has been used to describe the relationship between the dendrite growth rate, V_d, and the undercooling ΔT_d for a given alloy and solute concentration [20]. In hypoeutectic binary Al–Si alloys, the values reported for the exponent b are within the range of 2.5–3 for undercoolings near to those present during sand cast alloy solidification [20,21]. The use of this kind of expressions implies that for a given alloy composition, a log–log plot of the growth rate versus the undercooling should result in a linear relationship. For the relatively low undercooling present during sand casting, this kind of expression can be taken as a first approximation. In solidification processes where the operating undercoolings are considerably larger, like in rapid solidification, it has been shown [20] that the parameters b and B must be variable as a function of undercooling and solid/liquid interface composition.

During the primary phase growth simulation, the dendritic undercooling, ΔT_d, was calculated from the difference between the equivalent solute content at the solid/liquid interface corresponding to the dendrite tip, determined by using the instantaneous local temperature and the liquidus of the equivalent phase diagram, and the mean equivalent solute concentration in the liquid, calculated assuming perfect mixing in the liquid and absence of solute diffusion in the solid solution.

The rate of growth of eutectic grains was calculated using the relationship:

$$\frac{\partial R_E}{\partial t} = \mu_E \Delta T_E^2 \quad (4)$$

where R_E is the radius of the eutectic growing grains, μ_E is the eutectic growth constant and ΔT_E is the eutectic undercooling.

The effect of grain impingement on the solidified volume is taken into account using [9] the Jhonson–Mehl approximation to describe the solid fraction:

$$f_s = 1 - \exp(aR^n) \quad (5)$$

where $a = (4/3)\pi N$ and $n = 3$, in the case of N solid spheres of mean radius R, growing in a unit volume of solid/liquid system.

If it is considered that during the growth of the primary phase the dendritic grains are semisolids, and assuming that f is the solid dendrite fraction within a given semisolid dendritic grain of radius R_d, where f is approximately of the order of 0.2–0.4 [22], then the solid fraction during dendritic growth can be expressed as:

$$f_s = 1 - \exp(-faR_d^n) \quad (6)$$

In the hypoeutectic A_1 alloy, during eutectic solidification, the eutectic grows in the interdendritic and the intergranular regions of the primary phase solid network, and the impingement of the growing eutectic with the preexistent solid can significantly delay the growth process [23]. During simulation of A_1 alloy eutectic solidification, the eutectic growth rate is decreased multiplying the Eq. (4) by the factor $(1-f_s)^{xf_s}$, with $x = 2$, to take into account this delay. The use of this factor enables the generation of simulated cooling curves with a shape closer to that obtained from experimental measurements at the latter stages of A_1 alloy solidification. The numerical determination of the solid fraction evolution was performed using the simplified method outlined in Ref. [9].

The secondary dendrite arm spacing, SDAS, was obtained from Eq. (7), where t_s is the local solidification time and the ripening parameter M is of the order of 5.3×10^{-18} m^3 s^{-1} [24].

$$SDAS = 5.5(Mt_s)^{1/3} \quad (7)$$

The instantaneous interlamellar spacing, λ_{Eu}, was calculated using Eq. (8), where ε, the interlamellar coefficient, is of the order of 3.4×10^{-8} $m^{3/2}$ $s^{-1/2}$ [15,25]:

$$\lambda_{Eu} = \left[\frac{\varepsilon}{\Delta T_E \sqrt{\mu_E}} \right] \quad (8)$$

The coupling between macroscopic heat flow and solidification kinetics models was achieved by using a fully two way coupling, as described by Sasikumar [26]. The Eq. (1) was solved by the implicit finite difference method. During solidification, the local changes in the solid fraction within the casting are calculated at the beginning of every interval of time by inputting the temperature field at this time into the solidification kinetic model. The results obtained are then used during the calculation of the next temperature field.

This model was used to generate simulated cooling curves in the conditions corresponding to the experimental measurements. The thermophysical data used during calculations are shown in Table 2.

Table 5
Experimental conditions and thermocouple locations

Alloy	Pouring temperature (°C)	Thermocouple locations (m)	
		r^1	r^2
A_1	720	0.0005	0.004
A_2	680	0.0005	0.004

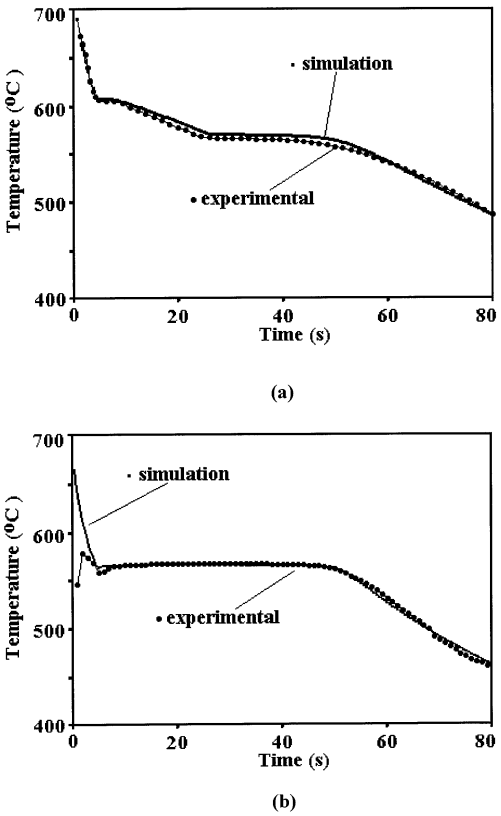

Fig. 1. Predicted and measured cooling curves at the inner ($r = 0.005$ m) thermocouple position for: (a) hypoeutectic A_1 alloy; (b) A_2 eutectic alloy.

3. Results and discussion

The pouring temperature of the experimental alloys and the thermocouple locations are shown in Table 5. The resulting cooling curves (T versus t) for the inner thermocouple position, obtained during the cooling and solidification of the A_1 and A_2 alloys are shown respectively in Fig. 1a and b. The predicted cooling curves according to the solidification model are also shown on these figures. From Fig. 1 it can be seen that a reasonably good agreement is exhibited between the experimental and the predicted cooling curves. The quantitative discrepancies observed in Fig. 1a, indicates the presence of factors not captured by the model. This might be related to the simplifications assumed in the model and to limitations in the thermophysical parameters used.

The metallographic observations of the SDAS as a function of radial position in A_1 alloy probe indicates the presence of a frame of approximately 600 μm in width, at the immediate neighborhood of the metal/mold interface where it can be observed an evident diminution of SDAS when compared with the coarser spacing present in the internal region of the probe, where the SDAS remains apparently the same. Accordingly, Fig. 2 shows, for the A_1 alloy, the dendritic spacing observed at the center of probe, Fig. 2a, and at the edge of the probe, Fig. 2b, where the dark zone delimitates the edge of the probe. Note at the upper right corner of Fig. 2b, the presence of SDAS similar to those shown in Fig. 2a. The measured SDAS mean values in the regions of interest were 35.3 ± 3.2, 35.1 ± 2.2 and 29.4 ± 1.1 μm, for the central region, the intermediate region and the edge region, respectively. The predicted SDAS values in A_1 rod casting are shown in Fig. 3 as a function of the radial position. The plotted results where obtained taking into account the predicted local solidification times and the Eq. (7). The measured SDAS are also shown in this figure, where it can be observed a qualitative agreement between the experimental and predicted trends. The quantitative discrepancies observed on Fig. 3 might be related to the difference between experimental and predicted local solidification times, to the limitations of the coarsening model [28] implicit in Eq. (7), including the applicability of the selected ripening parameter to the case of the experimental A_1 alloy, or to experimental errors associated to the SDAS measurement method [14], used in this work.

For the A_2 alloy, the metallographic observations indicate that the trend of interlamellar eutectic spacing as a function of radial position from the edge to the center of the probe is as follows: very narrow interlamellar spacings at the edge of the casting followed by an intermediate zone showing coarser spacings and relatively thick silicon flakes. Finally at the thermal

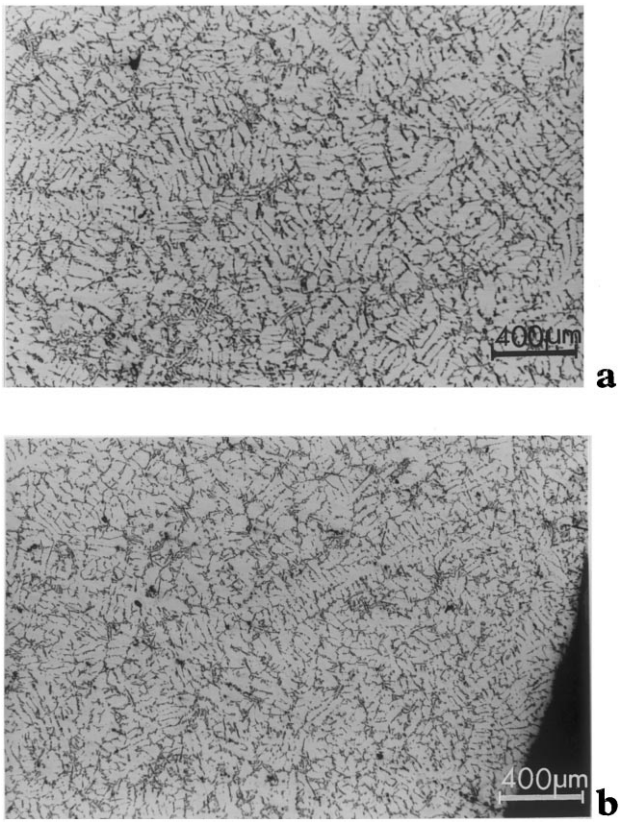

Fig. 2. Secondary dendrite arm spacings, SDAS, observed in A_1 alloy rod casting at: (a) center of the probe, $r = 0$ m; (b) edge of the probe, $r = 0.008$ m.

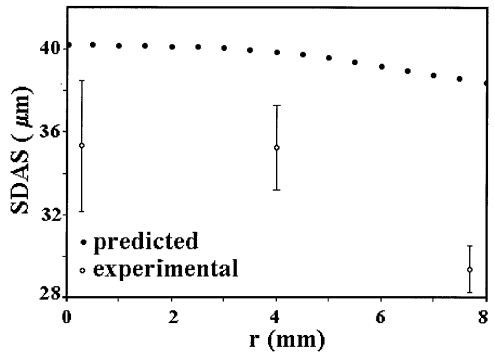

Fig. 3. Variation of the SDAS as a function of the radial position within the casting.

center of the casting very narrow interlamellar spacings are found again. Fig. 4 shows the interlamellar spacings in the central region, near to the symmetry axis of the casting (Fig. 4a), the external region, in the immediate neighborhood of the metal/mold interface (Fig. 4b) and in the intermediate region (Fig. 4c). The mean interlamellar eutectic spacing measured in the regions of interest were 3.4 ± 0.4, 3.1 ± 0.3 and 7.2 ± 0.7 μm, for the central region, the edge region, and the intermediate region, respectively. The predicted variation of the local interlamellar spacings as a function of the solidified fractions at the three locations selected for metallographic examination in A_2 alloy probe is shown in Fig. 5. Here, it can be seen that almost half of the solid formed at the thermal center of the rod casting, (s, Fig. 5), reaches interlamellar spacings that are similar and even lower than the interlamellar spacings occurring at the edge of the probe, (i, Fig. 5), which in turn indicates that the last liquid solidifying in the center of the casting, solidifies under large undercooling conditions.

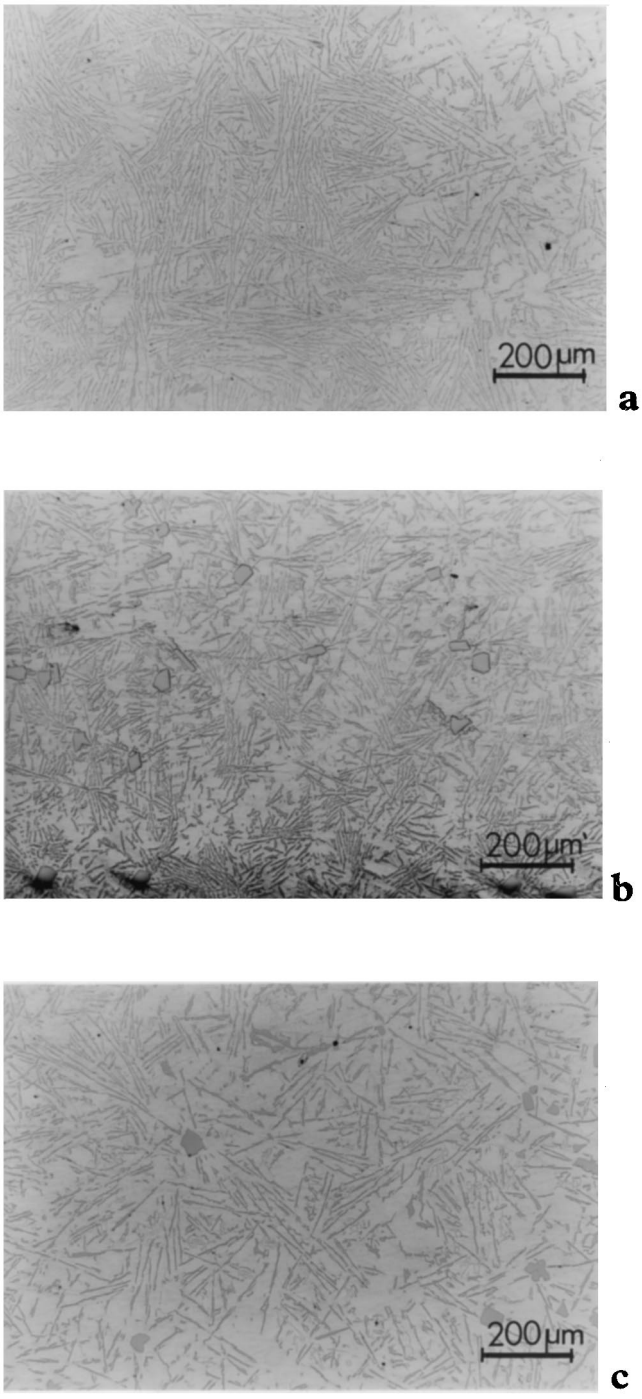

Fig. 4. Interlamellar eutectic spacings in different positions of the A_2 alloy rod casting: (a) central region, $r = 0$ m; (b) external region, $r = 0.008$ m; (c) intermediate region, $r = 0.004$ m.

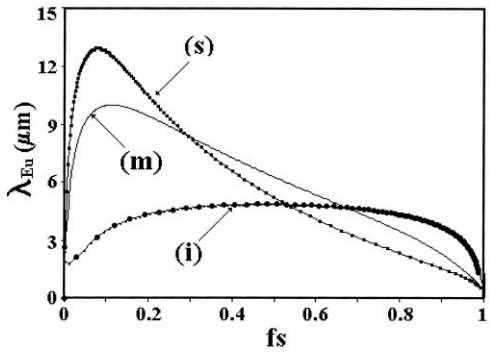

Fig. 5. Evolution of the predicted interlamellar eutectic spacings as a function of the solid fraction at: center of the probe, s, $r = 0$ m; edge of the probe, i, $r = 0.008$ m; intermediate position, m, $r = 0.004$ m.

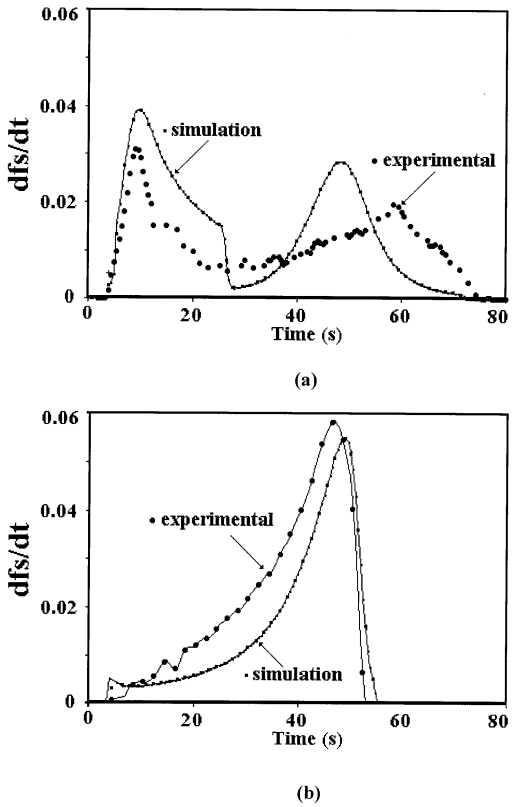

Fig. 6. Solidification rates obtained from FTA processing of the experimental and predicted cooling curves for: (a) A_1 alloy rod casting; (b) A_2 alloy rod casting.

With regard to the measured mean grain size of the hypoeutectic and the eutectic alloy probes, it is found, when compared to the model predictions, a good agreement, as expected, because the related grain count values were also included for the calculation of the empirical nucleation laws used during simulation. For the hypoeutectic A_1 alloy, the measured and the predicted mean grain sizes were 517 and 550 μm, respectively. In the case of the eutectic A_2 alloy, the measured and the predicted mean grain sizes were 1150 and 1160 μm, respectively.

In order to obtain local solidification kinetics information, related to the metal region near to the inner thermocouple, using the experimental data, the experimental cooling curves where numerically processed using the FTA method [8]. The simulated cooling curves were also treated by using this method.

The solidification rates obtained from FTA processing of the experimental and predicted cooling curves are shown in Fig. 6. The local solidification rates shown in this figure are related to the solidification events that occur in the central region of the rod castings. It can be seen on this figure that the evolution of the solidification rate trends is different for the hypoeutectic and the eutectic alloy. In Fig. 6a, associated to the hypoeutectic A_1 alloy, it can be observed the presence of two maxima. The first maximum corresponds to the solidification of the primary phase and the second is related to the eutectic solidification. The valley situated between the maxima indicates that there is a period of time, during the solidification of the central region of the A_1 alloy casting, when the solid formation becomes more difficult. This period of time corresponds to the initial stage of eutectic solidification, Fig. 1a, between $t = 25$ s and $t = 40$ s in both the predicted and the experimental FTA results. Similar trends have been reported for FTA results of hypoeutectic cast iron [8]. In Fig. 6a, the discrepancies between simulated and experimental trends during eutectic solidification of the hypoeutectic alloy shows that a further improvement is needed to simulate the solidification kinetics of the eutectic growing in the interdendritic zones.

The solidification rates obtained from the FTA method for the A_2 alloy shows an initial maximum of a relatively small magnitude followed by a significantly larger second maximum, attained almost at the end of solidification (Fig. 6b). The trend and shape of the solidification rates obtained shows a close resemblance with the results obtained from FTA processing of cooling curves associated to other eutectic system alloys, in particular for eutectic gray cast iron [6,8].

Regarding Fig. 6b at the initial stage of solidification, the relatively slow operating solidification rate produce a slow solid fraction increment which shows an initial restriction for solidification development in the central part of the casting. This restriction is progressively eliminated as the solidification of the cast reaches the end.

In order to explain, based on experimental information, the presence, at the thermal center of the A_2 alloy rod casting, of a refined eutectic structure, Fig. 7 shows the solid fraction and derivative cooling curve evolution obtained from FTA processing of the experimental A_2 alloy cooling curves. Here, it can be observed that the last liquid solidifying in the central part of the casting solidifies under a more negative cooling rate promoting large undercooling in this zone.

Accordingly, Fig. 8 shows the experimental solid fraction obtained from FTA method and the experimental apparent eutectic undercooling (i.e. the eutectic undercooling calculated taking into account the maximum recalescence temperature instead of the eutectic temperature) as a function of time. The eutectic growth theories [12,25], indicates that an increase in the operating undercooling during solidification promotes a finer eutectic microstructure, with narrow spacings between

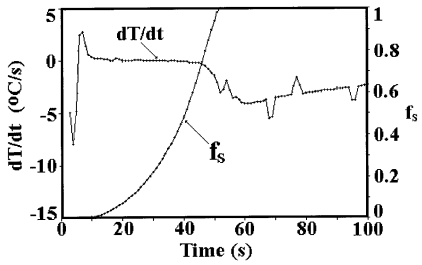

Fig. 7. Derivative of the experimental cooling curve and volume fraction of solidified A_2 near eutectic alloy at the center of the rod casting using FTA method.

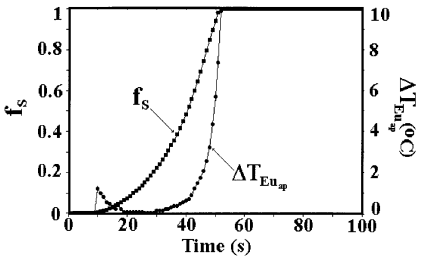

Fig. 8. Evolution of the experimental volume fraction of solidified Al–Si eutectic alloy, f_s, using FTA method, and of the apparent eutectic undercooling in the central region of the casting.

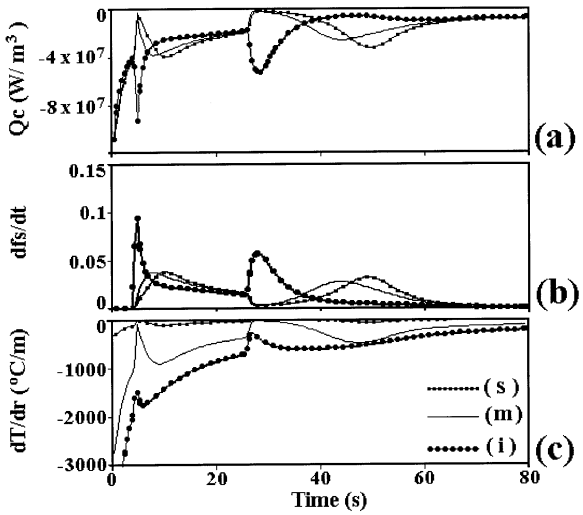

Fig. 9. Model predictions for the solidification rate, df_s/dt, the volumetric heat flow dissipated, Q_c, and the thermal gradient, dT/dr, as a function of time considering three positions inside the A_1 casting alloy: s, $r = 0$ m; i, $r = 0.008$ m and m, $r = 0.004$ m.

eutectic lamellae. Hence, FTA results indicates the presence in the thermal center of the A_2 alloy casting, of a liquid metal that solidifies under an increasing degree of undercooling, and this in turn implies the presence in this zone of fine and narrowly spaced eutectic silicon flakes as shown by metallographic findings (see Fig. 4a). Similar effects have been shown by other eutectic alloy systems. In eutectic gray cast iron [7,27] the presence of microstructural length refinement in the region near to the thermal center of the casting has been explained as an effect of the increasing degree of undercooling in the final solidifying liquid metal.

In order to enable the reaching of a proposal intended to explain the trends shown by the SDAS in A_1 alloy and by the interlamellar eutectic spacing found in A_2 eutectic alloy, as a function of the radial position in the experimental rod castings, it is interesting to explore the process phenomenology through the examination of the interdependence existing between the various features associated whit the solid fraction evolution in different locations within the metal, as revealed by the model. The link between microstructural and solid fraction evolution features can be achieved because the local solidification rate evolution is related to the local undercooling present during solid formation. In this regard, the dendritic and eutectic growth theories [11,12] show that as the undercooling is increased, there is an increase in the solidification rates and a decrease in the microstructural lengths of the solid formed. Furthermore it has been shown that the dendrite arm spacings observed in the solidification products depends on the undercooling present during dendrite formation and on the time available for coarsening [28]. High undercooling and short local solidification times are associated to finer dendrite arm spacings.

The solidification model prediction for the solidification rate, df_s/dt, the volumetric heat flow dissipated, Q_c, and the thermal gradient, dT/dr, as a function of time and position within the rod casting is shown in Figs. 9 and 10, for the A_1 and A_2 alloy, respectively. In these figures, s refers to the symmetry axis of the cylinder, $r = 0$ m, (i) to the metal/mold interface, $r = 0.008$ m and m refers to the intermediate region situated at $r = 0.004$ m. Note that the evolution of solidification rates and the thermal events occurring during A_1 and A_2 alloy solidification clearly depends on the relative position within the casting. Observing the concordance in time of the df_s/dt and the Q_c local evolutions during solidification, the Figs. 9 and 10 also shows a very close dependence of the solid formation kinetics on the local heat transfer. As Q_c represents the heat flux exchanged from the local volume to its surroundings (see Eq. (1)), the model outcome indicates that local solidification depends on the possibility of latent heat extraction from the local volumes to the external zones of the system. This in turn is restricted by the low heat

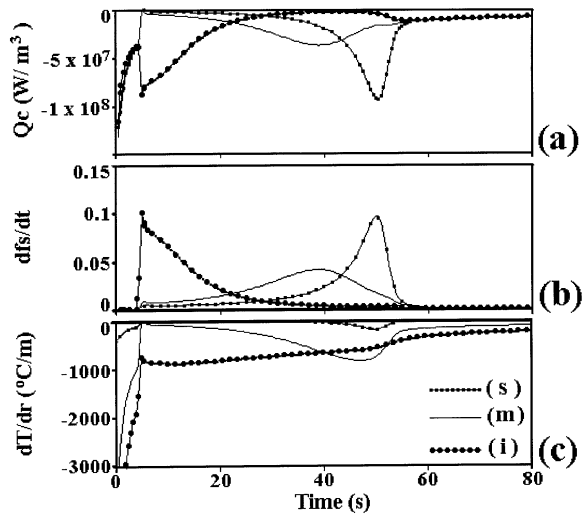

Fig. 10. Model predictions for the solidification rate, df_s/dt, the volumetric heat flow dissipated, Q_c, and the thermal gradient, dT/dr, as a function of time considering three positions inside the A_2 casting alloy: s, $r = 0$ m; i, $r = 0.008$ m and m, $r = 0.004$ m.

extraction capacity of the sand mold. It is known that the heat extracted from the casting is controlled by the low thermal diffusivity of the sand mold [21]. The amount of heat that can be transferred through the mold imposes a dynamical restriction on the cooling casting kinetics. When the region near to the metal/mold interface, during the cooling process, reaches the liquidus temperature, A_1 alloy, or the eutectic temperature, A_2 alloy, the local solidification starts. As the latent heat released can not be easily transferred to the mold, as a result of the restrictions mentioned above, the heat accumulation in this region produces changes in the thermal gradients, dT/dr, acting within the casting, as can be seen on Figs. 9c and 10c. This in turn modifies the heat exchanges between the different regions of the casting (Q_c in Figs. 9a and 10a), and controls the solidification evolution (Figs. 9b and 10b), the local operating undercooling and the microstructural characteristics of the solid formed at different positions within the casting.

The results depicted by the model in Fig. 10b, between $t = 6$ s and $t = 55$ s, for the near eutectic A_2 alloy, shows solidification rate trends that are similar to those predicted during the eutectic solidification of A_1 alloy, Fig. 9b, between $t = 26$ s and $t = 55$ s. Furthermore the relative magnitudes of the maximum local solidification rates observed in Fig. 10b indicates that the undercooling acting when solidification develops more intensively in the external, i, and in the central region, s, of the A_2 alloy casting are larger than those present during the solidification of the intermediate region of the casting. This implies finer interlamellar eutectic spacings at the edge and in the center of the casting than those present in the intermediate region, as shown by the metallographic findings (see Fig. 4).

It can be seen on Fig. 10c, between $t = 6$ s and $t = 20$ s, that during eutectic solidification of the outer zone, i, the thermal gradients acting in the inner zones of the casting, m and s, reaches and remains at values near to zero, slowing very steeply the corresponding solidification rates, until most of the latent heat released by the eutectic solidification of the outer zone i, see Fig. 10a, is dissipated through the metal/mold interface. This might be associated to the near isothermal nature of eutectic solid formation, which restricts during eutectic solidification, the temperature present at the outer zone of the casting to an approximately constant value, until this zone is capable to decrease its temperature, which occurs when the heat extracted by the sand mold at the metal/mold interface is larger than the latent heat released in the outer zone of the casting plus the heat arriving to this zone from the inner part of the casting, see Eq. (1). This implies a clear sequential nature, from the edge to the center of the casting, of the eutectic solid formation. It can be shown that 84% of the total metallic mass of the cylindrical casting is situated between $0.4R_{tot}$ and R_{tot}, where R_{tot} is the total radius of the cylindrical casting. When the last liquid batch, at the thermal center of the casting, develops more intensively its solidification, there is an enveloping solid metal shell in a stage of cooling, extracting important amounts of heat from the central region. As the amount of latent heat released as a result of the last liquid batch solidification is relatively insignificant, because of the reduced mass involved (for instance, only 1% of the total casting volume is situated between $r = 0$ and $r = 0.1R_{tot}$), the local temperature falls, causing that the last solidifying liquid in the thermal center solidifies under an increasing undercooling, with the microstructural consequences shown in Fig. 4a. Thus the presence at the thermal center of the casting of a liquid alloy that can achieve considerable undercooling during the last stages of solidification, may be explained as a result of the evolution of the internal thermal gradients acting during the eutectic solidification process, and to the metallic mass distribution from the center to the edge of the casting. In this regard it has been mentioned [7,27] that the occurrence of this effect depends on the geometry of the casting, the highest possibility happening in the thermal center of spherical castings and the lowest one in planar castings.

In the case of the primary phase dendritic solidification, it can be seen, Fig. 9c, between $t = 6$ s and $t = 25$ s, that the latent heat accumulation associated to the initial stages of the dendritic solidification in the outer zone change the thermal gradient acting in the inner zones m and s of the casting, which instantaneously reaches values near to zero, slowing the corresponding solidification rates. However and as the development of the dendritic solidification in the outer zone implies the continuous decrease of the local temperature (as a result of the decrease of the operant liquidus temperature

associated to the solute enriched liquid in contact with the growing solid/liquid interface), the thermal gradient trend shown by the internal regions indicates a relatively fast return to more negative values after the initial stages of the dendritic solidification of the outer zone of the casting. It can be observed in Fig. 9b, at the initial stage of the primary phase solidification, i.e. between $t = 6$ s and $t = 9$ s, that the higher solidification rates are reached in the outer zone (i). Afterwards, the solidification rates trend of the three regions i, m and s shows values that are similar and these situation stays until the reaching of the eutectic temperature. This show that the solid formation associated with dendritic solidification develops almost simultaneously in all the regions of the casting, in contrast with the sequential nature of eutectic solidification mentioned above. When the hypoeutectic casting reaches the eutectic temperature, which occurs almost simultaneously in the three regions considered for the analysis, eutectic solidification of the interdendritic liquid starts, and according to the concepts discussed above for eutectic solidification, the eutectic solidification of the outer zone of the casting ends at times shorter than those present at the inner regions. As can be seen on Fig. 9b, the initial high solidification rates and in consequence, the initial large undercooling present during the formation of the dendrites growing in the outer zone, and the lower solidification time associated to the earlier eutectic solidification of this zone may explain the presence, in the immediate neighborhood of the metal/mold interface, of SDAS smaller than those present at the inner regions of the casting. Also it can be observed in Fig. 9b, from the solidification rate evolution of the inner regions s and m during the primary phase solidification, that the undercooling acting in the inner regions are similar. Also it can be seen on this figure that the local solidification times related to s and m are very close. From this, it can be expected to find similar SDAS values in both zones, larger than the spacings present at the edge of the casting. These observations are in agreement with the metallographic findings on the trend showed by the SDAS as a function of the radial position.

Finally, it should be cautioned, with regard to the assumptions used in this work, that the roll of fluid flow on the effects discussed above must be established. It is expected that in the case of more complex castings, the effect of fluid flow during solidification might play an important roll on the final microstructure observed in the casting.

4. Conclusion

(1) The local solidification kinetics obtained from FTA processing of the experimental cooling curves under the conditions present in this work indicates that the evolution of the solidification rate trends in the central part of the rod castings is different for the hypoeutectic and the eutectic Al–Si alloys.

(2) The characteristic microstructural lengths depend on the radial position in the cylindrical casting. For the eutectic alloy the observed trend is as follows: very narrow interlamellar eutectic spacings at the edge of the probe followed by an intermediate zone showing coarser spacings and relatively thick silicon flakes. Finally, at the thermal center of the casting very narrow interlamellar spacing are found again. For the hypoeutectic alloy the observed trend of secondary dendrite arm spacing is as follows: narrow SDAS at the immediate neighborhood of the edge of the probe followed by coarser SDAS, apparently uniform in the rest of the probe.

(3) Comparing the experimental results with the predictions of the simulation solidification model used in this work, it can be observed a close resemblance between the shape of the experimental cooling curves and solidification rate trends with those obtained from the Fourier analysis of the predicted cooling curves. Also the microstructural findings are in agreement with the trends predicted by the model.

(4) The model and experimental results, including FTA results and metallographic observations suggest that there is a strong dependence of local solidification kinetics on local heat transfer, and the analysis of this dependence may be used to explain the observed changes of microstructural characteristics at different locations within castings.

(5) The model outcome shows that the heat extraction restriction imposed by the low thermal diffusivity of the sand mold produces, during solidification, changes in the internal thermal gradients acting in the different positions of the casting. This in turn regulates the energy exchanges of the local regions of the casting and controls the local solidification kinetics, the local operating undercooling and the microstructural characteristics of the solid formed at different positions within the casting.

(6) The results of this work suggest that in the case of solidification products that were formed in a wide temperature interval, as in equiaxed dendritic solidification of primary phases, it is expected to find a gradual decrease of the corresponding characteristic microstructural lengths from the thermal center to the metal/sand mold interface. In the other hand, in the case of solidification products that were formed in a very narrow temperature interval, as is the case of eutectics, it may be present an effect of microstructural length refinement at the thermal center of the casting.

Acknowledgements

The authors would like to acknowledge to the DGAPA, UNAM, for the financial support (Project IN501596) and to I. Beltran and C. Atlatenco for their valuable technical assistance.

Appendix A. Notation

Cp^{v} Volumetric heat capacity (J m^{-3} °C)
C_{0i} Initial solute content (wt%)
f_s Solid fraction
h Convective heat transfer coefficient (W m^{-2} °C)
k^{th} Thermal conductivity (W m^{-1} °C)
k_i Partition coefficient of solute i
L_f^v Volumetric latent heat (J m^{-3})
m_i Liquidus slope associated to solute i (°C $wt\%^{-1}$)
$\hat{N}$ Volumetric grain density (m^{-3})
Q_a Volumetric heat accumulation flow (W m^{-3})
Q_c Volumetric heat dissipation flow (W m^{-3})
Q_s Volumetric latent heat generation flow (W m^{-3})
Radial position (m)
Temperature (°C)
Time (s)
V_d Dendrite tip velocity (m s^{-1})
ΔT_d Dendritic undercooling (°C)
ΔT_E Eutectic undercooling (°C)

λ_{Eu} Eutectic interlamellar spacing, m

References

[1] D.M. Stefanescu, ISIJ Int. 35 (6) (1995) 637.
[2] L. Nastac, D.M. Stefanescu, Metall. Mater. Trans. A 27A (1996) 4061.
[3] T. Kraft, H.E. Exner, Z. Metallkd 87 (7) (1996) 598.
[4] G. Upadhya, A.J. Paul, AFS Trans. 102 (1994) 69.
[5] T. Kraft, Model. Simul. Mater. Sci. Eng 5 (1997) 473.
[6] E. Fras, W. Kapturckiewicz, A. Burbielko, H.F. Lopez, Metall. Mater. Trans. B 28B (1997) 115.
[7] E. Fras, W. Kapturckiewicz, A. Burbielko, H.F. Lopez, AFS Trans. 104 (1996) 1.
[8] E. Fras, W. Kapturckiewicz, A. Burbielko, H.F. Lopez, AFS Trans. 101 (1993) 505.
[9] E. Fras, W. Kapturckiewicz, H.F. Lopez, AFS Trans. 100 (1992) 583.
[10] C. González-Rivera, H. Cruz M, A. García, J. Juarez-Islas, J. Mater. Eng. Perf. 8 (1) (1999) 103.
[11] W. Kurz, D.J. Fisher, Fundamentals of Solidification, TransTech Publications, Switzerland, 1984.
[12] R. Trivedi, W. Kurz, Acta Metall. Mater. 42 (1) (1994) 15.
[13] J.O. Barlow, D.M. Stefanescu, AFS Trans. 105 (1997) 349.
[14] L. Backerud, E. Krol, J. Tamminen, Solidification Characteristics of Aluminium Alloys, vol. 1, AFS/Skanaluminium, 1990.
[15] P. Magnin, J.T. Mason, R. Trivedi, Acta Metall. Mater 39 (4) (1991) 469.
[16] D.M. Stefanescu, G. Upadhya, D. Bandyopadhyay, Met. Trans. A 21A (1990) 997.
[17] H.P. Wang, J. Zou, E.M. Perry, R. Doherty, AFS Trans. 101 (1993) 771.
[18] M. Rappaz, P. Thevoz, Acta Metall. 35 (7) (1987) 1487.
[19] J. Lipton, M.E. Glicksman, W. Kurz, Mat. Sci. Eng. 65 (1984) 57.
[20] J. Lipton, W. Kurz, R. Trivedi, Acta Metall. 35 (4) (1987) 957.
[21] M. Flemings, Solidification Processing, McGraw Hill, New York, 1974.
[22] I. Dustin, W. Kurz, Z. Metallkd. 77 (1986) 265.
[23] S. Chang, D. Shangguan, D.M. Stefanescu, Met. Trans. A 23A (1992) 1333.
[24] J. Zou, S. Shivkumar, D. Apelian, AFS Trans. 97 (1990) 871.
[25] P. Magnin, R. Trivedi, Acta Metall. Mater. 39 (4) (1991) 453.
[26] R. Sasikumar, M. Kumar, Acta Metall. Mater. 43 (12) (1995) 4387.
[27] E. Fras, W. Kapturckiewicz, A. Burbielko, Modeling of Casting, Welding and Advanced Solidification Processes VI, The Minerals, Metals and Materials Society, TMS, 1993, p. 261.
[28] A. Mortensen, Metall. Trans. A 22A (1991) 569.